A Handheld High-Sensitivity Micro-NMR CMOS Platform with B-Field Stabilization for Multi-Type Biological/Chemical Assays

Ka-Meng Lei [1], Hadi Heidari [2,3], Pui-In Mak [1], Man-Kay Law [1], Franco Maloberti [2], Rui P. Martins [1,4]

1 - State-Key Laboratory of Analog and Mixed-Signal VLSI and FST-ECE, University of Macau, China
2 - University of Pavia, Italy 3 - now with University of Glasgow, United Kingdom
4 - On leave from Instituto Superior Técnico, Universidade de Lisboa, Portugal

E-mail Correspondence: Pui-In Mak, pimak@umac.mo

Abstract

We report a micro-Nuclear Magnetic Resonance (NMR) system compatible with multi-type biological/chemical lab-on-a-chip assays. Unified in a handheld scale (dimension: 14 x 6 x 11 cm^3, weight: 1.4 kg), the system is capable to detect < 100 pM of *Enterococcus faecalis* derived DNA from a 2.5-µL sample. The key components are a portable magnet (0.46 T, 1.25 kg) for nucleus magnetization, a system PCB for I/O interface, an FPGA for system control, a current driver for trimming the magnetic (B) field, and a silicon chip fabricated in 0.18-µm CMOS. The latter, integrated with a current-mode vertical Hall sensor and a low-noise readout circuit, facilitates closed-loop B-field stabilization (2 mT $\rightarrow$ 0.15 mT), which otherwise fluctuates with temperature or sample displacement. Together with a dynamic-B-field transceiver with a planar coil for micro-NMR assay and thermal control, the system demonstrates: 1) selective biological target pinpointing; 2) protein state analysis and 3) solvent-polymer dynamics, suitable for healthcare, food and colloidal applications, respectively. Compared to a commercial NMR-assay product (Bruker mq-20), this platform greatly reduces the sample consumption (120x), hardware volume (175x) and weight (96x).

Index Terms

Baseband, biological, biosensor, chemical, CMOS, deoxyribonucleic acid (DNA), filter, Hall sensor, immunoglobulin, lab-on-a-chip, low-noise amplifier (LNA), magnetic sensing, nuclear magnetic resonance (NMR), point-of-care, polymer, power amplifier (PA), protein, radio frequency (RF), receiver (RX), transceiver (TRX), transimpedance amplifier (TIA), transmitter (TX).

I. Introduction

Point-of-use (PoU) biological/chemical assays offer a prospect to modernize the bulky laboratory instruments into easy-to-use lab-on-a-chip platforms, bringing down the cost, size and sample-use by orders of magnitude [1]. Beyond them, it is also tantalizing to develop a unified PoU platform apt for different application-specific assays [2]. Particularly for biomolecule target detection, the capability of the assay to sense the biomolecules specifically and selectively facilitates early disease detection [3]. From the report of the World Health Organization (WHO), almost 1/3 of reported death in low-income countries in 2012 was attributed to infectious diseases (i.e., HIV/AIDS, Malaria, Tuberculosis, etc.) [4]. Yet, conventional centralized detection techniques (e.g., qualitative polymerase chain reaction and enzyme-linked immunosorbent assay) can have a long turnaround time and demand skillful operators. These restrictions perplexed rapid detection of contagious diseases, and made it a Herculean task for governing the fierce spreading of the epidemic in rural and resource-limited regions.

Scientists and engineers have been intensively investigating multifarious of *in vitro* biosensors for rapid disease diagnosis [5]. For instance, the prevailing lateral flow assay is notable for its simplicity and inexpensiveness [6]. Yet, its qualitative or semi-quantitative results limit their usages to only preliminary assays [7]. On the other hand, CMOS chips are promising for rapid and quantitative detection at low cost [8]. The evolution of CMOS technologies and the improvement of circuit techniques led to the success of CMOS chips in the delicate biomedical arena and a wide variety of CMOS-based diagnosis platforms for *in vitro* biomolecule detection based on different transduction mechanisms becomes a reality [9]. For instance, a CMOS fluorimeter detects fluorescent light from labeled biomolecules [10]. Upon the excitation by an external light source, the fluorescent dyes such as Cy3 and Cy5 emit signals for detection by the CMOS chip. Yet, the labeling process and external modules (i.e., optical filter and excitation light source) confound the operations and degrade its portability. Alternatively, the electrical properties such as impedance [11] or charge flows [12], [13] of the samples can reliably reflect the biological reactions. Their direct and label-free

detections circumvent from experimental uncertainty attributed to the perplexity of label on the target, thus reducing the time and labor effort. These electrical-based transducers ineluctably include a recognition probe on the electrode to selectively detect the target of interest. When the target analytes bind with the recognition probe, the transducers convert this event into a measurable electrical signal. The implementation of the recognition layer, however, requires certain chemical post-processing steps, thereby stiffening the preparation step for the assay. Instead, by employing bio-compatible magnetic particles, CMOS chips are also capable of detecting the targets inside the samples by magnetic-sensitive transducers such as Hall sensors [14] or Giant magnetic resistive spin-valve sensors [15]. As their magnetic particles are labeled on the probe, this quasi labeling-free sensing scheme embellishes the standard surface modification procedure of target labeling [16], simplifying the sample preparation. Compared to the impedometry, the post-processing step on the CMOS chip can be relieved as direct contact between the sample and CMOS chip is averted. Yet, recognition elements are still entailed to immobilize on a surface in proximity of the transducer for high sensitivity. Therefore, the desired sensing scheme should entail neither complex sample preparation, nor chemical post-processing steps on CMOS chip to achieve rapid and low-cost target detection.

Nuclear Magnetic Resonance (NMR) is powerful to explore the sample information at the molecular level. The underpinning physics of NMR is the exchange of energy between the RF magnetic field and spin of the non-zero spin nuclei. By exploiting functionalized magnetic nanoparticles (MNPs) as the probe, the NMR-based quasi label-free detection scheme can pinpoint a broad range of unprocessed biological targets such as DNA [17] and protein [18]. Although NMR is known for its relatively low sensitivity, the MNP here provides inherent signal amplification to NMR since a single MNP cluster can affect billions adjacent water molecules [19]. Furthermore, unlike the aforesaid sensing schemes, screening by NMR is rapid and low-cost as it is quasi label-free for the samples, and immobilization-free for the transducers/electrodes. Such benefits render NMR-based detection as a promising solution for PoU applications. Recently, researchers have been focusing on miniaturizing the magnet of the NMR and

migrating the modular and complex electronics into CMOS chips [20]-[23]. These pathbreaking works significantly shrink the benchtop NMR equipment to a portable scale. Yet, ascribed to the thermal instability, the magnetic (B)-field variation of the magnet can easily paralyze the NMR experiment. This instability calls for a calibration scheme to enhance the robustness of the system.

Herein we report a handheld high-sensitivity micro-NMR CMOS platform utilizing a portable magnet (Fig. 1). A Hall sensor with low-noise readout circuit is embedded, for the first time in the literature, with a CMOS micro-NMR transceiver (TRX) to achieve better robustness. The current driver stabilizes the B-field of the magnet against ambient variation. The stabilized B-field avoids the need of a frequency synthesizer to tune the local oscillator (LO), and an untuned LO can be generated directly by the crystal oscillator (XO). The samples under assay are loaded on the on-chip planar coil by a handheld pipette. The sensing coil also serves as a sample heater for thermal profiling. Further, benefitting from the versatility of the NMR assays, this handheld tool unifies multi-type assays such as target detection, protein state analysis, and solvent-polymer dynamics, rendering it suitable for healthcare, food industry and colloidal applications.

This work was presented in *IEEE ISSCC* 2016 [24]. Here we disclose the entire design and engineering of the platform. Section II couches the challenges of the micro-NMR system and shows the system overview. Section III covers the design of the micro-NMR TRX, the Hall sensor, and its readout circuit. Section IV reveals the measurements and biomolecule experimental results, together with the benchmark with other CMOS bio-sensing platforms. Finally, Section V concludes the paper.

II. Challenges and System Overview

It is worth to discuss the key challenges of micro-NMR systems before introducing our micro-NMR CMOS platform. Relevant books [25] contain the detailed physics of the NMR. Micro-NMR relaxometry (i.e., measurement of the relaxation time of the samples) detects the spin-spin relaxation time (T_2) for the non-zero spin nuclei (i.e., ^{1}H, ^{13}C or ^{31}P). The nuclei magnetized by the static magnetic field (B_0) absorb an

orthogonal RF exciting magnetic field (B_1) at Larmor frequency, $f_L = \gamma B_0$, with the nucleus gyromagnetic ratio γ, and precess about the direction of magnetization at f_L even after the cessation of the excitation. Yet, the frequency deviation between the exciting pulse frequency (f_{EXC}) and f_L could paralyze the NMR experiment if f_L shifts away from the excitation pulses spectrum. Unlike superconducting magnets that can generate a stable B_0-field, small permanent magnets suffer from B_0-field variation due to temperature drift and displacement. For instance, the B_0-field from a Neodymium magnet can have a temperature coefficient of -1200 ppm/K. As such, f_L of the nuclei shifts together with B_0, imposing that calibration is essential to safeguard the system against environmental changes. Conventional frequency stabilization techniques are based on the measured NMR signals [22], [26], [27]. However, if the magnetic field fluctuates large enough such that the excitation pulses cannot excite the nucleus effectively, those calibration schemes may not work properly. Previously, we reported a calibration scheme to detect the ambient temperature and then tune the LO accordingly [28]. This method, however, suffers from a delay between the ambient temperature variation and the response on the magnet due to its high heat capacity (time constant >10 mins). Moreover, generating a tunable LO complicates the design of the platform.

A small permanent magnet also poses other challenges to the design of the TRX. As the SNR of the NMR experiment is commensurate with B_0 (i.e., Signal $\propto {B_0}^2$), the utilization of the small magnet demands a receiver (RX) with better sensitivity to counteract this signal loss. Additionally, the inhomogeneity of B_0 experienced by the sample entails a programmable transmitter (TX) for synthesizing specific pulse sequences to recover the incoherent spinning from the nuclei.

To circumvent the above challenges, the proposed micro-NMR platform (Fig. 2) includes B_0-field stabilization to enhance the robustness and simplify the hardware. The Hall sensor and readout circuit, together with an off-chip current driver, manage the lateral B_0-field and stabilize the bulk magnetization and thus f_L of the nuclei. The dynamic B_1-field transduction between the nuclei and the electronics is based on an on-chip planar coil driven by a TX/RX together with the matching capacitor C_M, to excite/obtain the magnetic signal to/from the droplet samples (2.5 μL) normal to the chip surface. Furthermore, the on-chip

NMR sensing coil can act as a sample heater for thermal profiling. A BJT-based temperature sensor aids both the Hall sensor thermal correction and thermal profiling of the samples.

III. Circuits Design

A. Micro-NMR Transceiver

The CMOS chip consists of a TRX for micro-NMR measurements. Starting from the TX, it delivers the pulse sequence to excite the nuclei, comprising an XO, a pulse sequence synthesizer (PSS) and a power amplifier (PA). This work entails an XO with an oscillation frequency 4x f_L to directly serve as the LO for both the TX and RX. This single-LO architecture eliminates the phase misalignment of the echo response caused by asynchronous LO, thus assuring a harmonized amplitude and phase of the echoes for peak-amplitude extraction. The XO with an inverter-based amplifier and an off-chip crystal (78.5 MHz) features low-power low-noise operation. Together with the proposed B_0-field stabilization, the TX avoids the need of a frequency synthesizer to generate a variable LO to track the unstable f_L. The signal from the XO is divided by 4 to provide the 4-phase LO for the PSS and mixers in the RX mode. The PSS flexibly generates different kinds of pulse sequences, such as the Carr-Purcell-Meiboom-Gill (CPMG) pulse [29], [30], according to the command from the FPGA (Fig. 3). The PA, based on class-D tapped inverter chains, delivers voltage pulses to the planar coil to excite the nuclei for the micro-NMR assay.

The generated micro-NMR signals are picked up by the RX that amplifies and downconverts them to the baseband. Ascribed to the moderate B_0 from the permanent magnet, the amplitudes of the micro-NMR signal are limited to a μV-level. Thus, to assure sensitive detection the RX entails a meticulous design, demanding an input-referred noise down to 1 nV/√Hz. To address it, a multi-stage low-noise amplifier (LNA) is employed to head the RX. Its complementary common-source architecture allows current-reuse and gain-doubling (gain: ~30 dB per stage). Following the LNA, a double-balanced quadrature mixer driven by the LO down-converts the amplified signals to the baseband. With a Gilbert-cell architecture, this active

mixer provides an additional gain (12 dB), and relaxes the noise requirement for the succeeding stages. After mixing, and to suppress the out-of-band noise and mixing products, a pair of I/Q dynamic-bandwidth lowpass filters (nominal cutoff frequency: 5 kHz) is adopted. Exhibiting a 6^{th}-order Butterworth response and implemented by a cascaded source-follower-based biquad [31], the lowpass filters feature area- and power-efficient operation (FoM = 128 fJ). The cutoff frequency is extended to 20 kHz during the TX mode for fast recovery from saturation after the excitation pulses [23]. This technique shortens the dead-time and strengthens the RX sensitivity [32]. The entire TRX, except the PSS, is differential to improve the immunity to external interferences.

B. Multi-Functional Planar Coil

An on-chip planar coil (23 turns, conductor width: 40 µm, spacing: 1.85 µm) transduces between magnetic signals from the nucleus spin in the axial direction and the electric signals of the TRX. This tiny coil miniaturizes the platform and sample consumption. To improve the quality factor of the coil (simulated Q = 1.9 at 19.6 MHz), a thick top metal (2.5 µm) and a stacked-metal-layer technique are applied. The coil in parallel with a capacitor forms an LC tank offering passive amplification for the signal (gain: $\sqrt{Q^2+1}$) [21]. Furthermore, to extend the functionality of this micro-NMR platform, the NMR-sensing coil is time-multiplexed to serve as a sample heater for thermal profiling. Modeled in COMSOL Multiphysics®, the entire temperature of the droplet uniformly raises (ΔT <0.3°C) according to the applied current on the coil [Fig. 4(a)]. The heating temperature is easily controllable by tuning the duty-cycle of the injected current [Fig. 4(b)]. A BJT-based temperature sensor monitors the sample temperature. It has a static temperature offset when reading the droplet temperature due to the physical separation, but the relative value adequately indicates the droplet temperature rise/drop activities. The design temperature rise (<20 °C) of the IC has negligible effect on the performance of the TRX, as verified by simulations.

C. Hall Sensor, Readout Circuit and Current Driver

The micro-NMR TRX integrates a Hall sensor to sense the B_0-field variation of the permanent magnet, which must appear orthogonally with the RF magnetic field. The detected B_0-field variation modulates the current passing through the auxiliary coil of the magnet to stabilize the resultant magnetic field, which allows system-level calibration.

Hall sensors can detect the magnetic field normal [33]-[35] or parallel [36], [37] to the chip surface. As the RF magnetic field generated by the planar coil is normal to the chip surface, the latter solution is required, which can be achieved by a vertical Hall sensor (VHS). Each VHS sub-element contains an n-well as the substrate, and three N-diffusions as contacts [Fig. 5(a)]. P-diffusions are embedded between the n-diffusions to avert the current flowing at the surface, soothing the *1/f* noise. This architecture renders the device with full standard CMOS compatibility. Working in the current mode implies the input is a constant current source (I_{Bias}) and outputs are two current terminals (I_P and I_N). When no external magnetic field exists, there is an equal split of I_{Bias} between I_P and I_N, which should be equal with no current difference.

When considering B_0 in the lateral direction (i.e., nominal to the cross-section of the VHS device), the charge carriers from the input terminal will experience a Lorentz force deflecting the charges, leading to non-identical magnitudes of I_P and I_N [Fig. 5(b)] expressed by:

$$I_P = \frac{I_{Bias}}{2} + I_{Hall}(B_0) \quad (1)$$

$$I_N = \frac{I_{Bias}}{2} - I_{Hall}(B_0) \quad (2)$$

where $I_{Hall}(B_0)$ is the induced Hall current on each output terminal commensurate with B_0. Thus, the measurement of I_{Hall} can determine B_0. Yet, the prodigious bias component I_{Bias} stiffens the measurement on I_P and I_N. To circumvent this measurement barrier, four identical VHS sub-elements $U_{1\text{-}4}$ are arranged to form a Wheatstone bridge (Fig. 6). The Wheatstone bridge prunes I_{Bias} at the output and only the B_0-dependent term I_{Hall} appears at the Wheatstone bridge's output. Furthermore, this

configuration not only features a fully-differential architecture, but also doubles the output Hall current improving the sensitivity of the VHS. A common-mode feedback circuit regulates the tail of the Wheatstone bridge, where two-phase spinning eliminates the effect of mismatch between the VHS sub-elements by periodically interchanging the output and supply terminals of the Wheatstone bridge (Fig. 7).

The induced differential current from the Wheatstone bridge ($I_{IN,P}$ and $I_{IN,N}$) is then converted to voltage for recording. Among multifarious options of transimpedance amplifier (TIA), a current integrator formed by a high gain amplifier with shunt integrating capacitor (C_F) appears as a promising solution, since it inherently offers lowpass filtering on the outputs without passive noise sources (e.g., feedback resistors for resistive feedback TIA), leading to a better noise performance [38] - [40]. Furthermore, the variation of the integration time T_{INT} will alter the gain of the fully-differential TIA, providing conversion flexibility (Fig. 8). The core of this TIA is a two-stage amplifier with a telescopic 1st stage, where the DC gain (A_{DC}, 100dB) guarantees accurate and stable operation (GBW = 100 MHz, PM = 50° at a 15-pF load), at a power budget of 2 mW excluding the bias circuit. A chopper deals with the offset and *1/f* noise of the amplifier with a chopping frequency of 1 MHz. This chopping technique reduces the *1/f* noise corner by 10,000× (from 200 kHz to 20 Hz) in an open-loop configuration. During the reset phase, $S_{1\text{-}4}$ nullify the residual voltages on C_F, while opening $S_{5\text{-}8}$ prevents the current to flow from the Wheatstone bridge into the TIA. In the measuring phase, $I_{IN,P}$ and $I_{IN,N}$ flow through $S_{7\text{-}8}$ and charge C_F, causing a complementary voltage ramp at the output of the TIA, expressed by (assuming an ideal TIA):

$$V_{OUT} = V_{OUT,P} - V_{OUT,N} = \frac{4I_{Hall}T_{INT}}{C_F} \quad (3)$$

For an ideal TIA, its input resistance ($R_{IN,TIA}$) should be zero to measure its input current accurately. The finite gain of the amplifier and the intrinsic resistances of the switches (R_{SW}), however, ineluctably exacerbate the performance of the TIA. Considering a TIA with *n* switches to regulate the current flow from the Wheatstone bridge and the spinning circuitry in its front, the average $R_{IN,TIA}$ below the resetting frequency ($1/T_{INT}$) should be:

$$R_{IN,TIA,conv} = \frac{T_{INT}}{A_{DC}C_F} + n \cdot R_{SW} \quad (4)$$

assuming a negligible reset time relative to T_{INT}. The first term on the right of (4) is the input impedance of the integrator whereas the second term emerges from the switches. While a multi-stage architecture can boost the gain of the amplifier at the expense of power consumption [41], the value of R_{SW} is limited to a certain range in a particular process since a large switch inextricably induces parasitic capacitance on the signal paths (Fig. 9). To this end, it is mandatory to diminish the effect of R_{SW} on the TIA. To achieve this, $S_{7\text{-}8}$ are managed to guide the current passing through the feedback paths, while avoiding switches between the TIA and Wheatstone bridge. $S_{5\text{-}6}$ provide connections between the input of the amplifier and the Wheatstone bridge. As long as there is no current (except leakage currents) flowing through $S_{5\text{-}6}$, the operation of the TIA will not be deteriorated. $R_{IN,TIA}$ in the proposed architecture is given by:

$$R_{IN,TIA,prop} = \frac{T_{INT}}{A_{DC}C_F} + \frac{n \cdot R_{SW}}{A_{DC}} \quad (5)$$

Where, in this switching scheme, A_{DC} represses the impact of the switches and allows the realization of a low input impedance TIA without creating a large parasitic capacitance at the signal paths. For example, $R_{IN,TIA,prop}$ = 171 Ω (simulated) with C_F = 8 pF, T_{INT} = 100 µs (gain: 250 V/µA) and R_{SW} = 240 Ω. When compared with the general approach that places 4 switches (2 for mastering and 2 for spinning) before the TIA [34], the suppression of $R_{IN,TIA}$ is now 85%, while the TIA absorbs ~20% more current (output impedance from Wheatstone bridge: 5 kΩ). The input-referred noise of the TIA is 10 pA/√Hz at 1 Hz, which is 79x better than the case without the chopper. After the measuring phase, the Hall currents from the Wheatstone bridge cease by switching off $S_{5\text{-}8}$, while turning on $S_{3\text{-}4}$ allows the reading of the voltage on C_F. The three-phase operation can be repeated and the results can be averaged to reduce the background noise.

The extension of T_{INT} produces an acceptable output level (e.g., LSB of the external ADC: 0.8 mV) induced by the B_0-field variation (3.75 mT). Yet, ascribed to the prodigious nominal B_0-field, a typical TIA can saturate and fail to sense this tiny B_0-field variation. The addition of a nominal B_0-field compensator implemented by a pair of switched-capacitor based current source with alternative phase (i.e., opposite current flow) is necessary to obviate this contrariety. During the measuring phase, the compensator nullifies the Hall current induced from the nominal B_0-field flowing into the TIA by generating and injecting the currents (I_{CAL+} and I_{CAL-}) into the TIA. Thus, there is only the integration of the variable part from the Hall sensors at the output of the TIA (Fig. 10), and by T_{INT} extension, more gain is achieved without saturating the TIA.

The current driver receives the converted results after digitization, and subsequently drives the auxiliary coil of the portable magnet and trims the B_0-field. Based on the Biot-Savart law, this injected current to the coil generates an additional magnetic field (75mT/A). This current modulates and stabilizes the actual B_0-field, which is the sum of the B_0-field from the permanent magnet and auxiliary coil [42], according to the results from the Hall sensor. The current driver implemented off-chip with discrete components prevents its interference (on-chip) due to the related high power consumption.

IV. Experimental Results

A. Electrical Measurements

Fabricated in the 1P6M 0.18-µm CMOS process, the chip occupies an area of 2.0 x 3.8 mm^2, dominated by the planar coil (dimension: 2.0 x 2.0 mm^2, L: 506 nH, Q: 1.84) as shown in Fig. 11(a). The dimension (14 x 6 x 11 cm^3) and weight (1.4 kg) of the system are dominated by the 0.46-T portable magnet (weight: 1.25 kg, diameter: 8 cm, height: 5.5 cm). In addition to the CMOS chip, there are a system PCB, a commercial FPGA (DE0-Nano) and a current driver [Fig. 11(b)]. A customized program on the PC controls the platform, simplifying the operation and visualization of the assay results [Fig. 11(c)]. The

computer extracts and evaluates the T_2 of the samples from the acquired signals. During the micro-NMR experiments, the RX mode consumes 22.1 mW dominated by the forefront LNA for high sensitivity. For the TX mode, the power consumption is 51.0 mW dominated by the PA that has a power efficiency of 31.6%. The VHS together with the readout circuit draw 8.4 mW. Both the TRX and Hall sensor parts switch into the idle mode after each assay to prolong the lifetime of the battery. With 2 AA batteries of 2.5 Wh capacity and a DC-DC converter efficiency of 90%, the system can finish up to 500,000 assays, assuming that the VHS is on for 1 second, then the NMR RX is on for 1 second (TX pulses are short such that the power of TX can be neglected in this case), and finally the entire system is idle for 9 seconds.

Before each micro-NMR assay, the Hall sensor is turned-on first with the VHS sensing the B_0-field (Fig. 12). As the B_0-field may shift away from its nominal value due to environmental variation (e.g., temperature and sample-to-magnet position), an untracked f_L can be easily off-center from f_{EXC} (BW: 16.7 kHz, equivalent to 0.5 mT in terms of B-field) and the operation of the platform can be paralyzed. With the proposed calibration scheme, the B_0-field variation is tracked by the VHS and readout circuit; they show a sensitivity of 4.12 V/T [Fig. 13(a)]. The eventual B_0-field is then balanced by modulating the auxiliary coil of the magnet with a particular magnitude of dc current, according to the result from the VHS and readout circuit. Thus, f_L can be reset to match with f_{EXC} to proceed the micro-NMR assay. Associated with signal-averaging performed in the frequency domain to suppress the background noise on the Hall sensor, the proposed calibration improves the B_0-field stability by 13× (from 2 to 0.15 mT) at 0.46 T nominal B_0-field (f_L = 19.6 MHz), corresponding to a variation on f_L of 6.9 kHz [Fig. 13(b)]. This variation is smaller than the BW of the excitation pulse, ensuring a secure micro-NMR operation. While this calibration scheme can handle large magnetic field fluctuation, the calibration for small magnetic field fluctuation such as [27] can also be performed in parallel to enhance the resolution if necessary.

The stabilized f_L allows the use of a simple XO as the LO, which measures low power (79 µW at V_{DD} of 0.9V) and low phase noise (-116 dBc/Hz at 1 kHz offset), as shown in Fig. 14(a) and (b), respectively.

B. Biological/Chemical Measurements

One of the crucial aims of this platform is to detect and quantify the biological target inside the samples for disease screening. For instance, considering Human Immunoglobulin G (IgG), which protects the body from infections by binding themselves to different pathogens. Protein A, which specifically binds Human IgG, used as a probe to detect the existence of IgG inside the samples by functionalizing them on the water-soluble MNPs ([Fe_2O_3]: 10 µg/mL, Ø: 25-30 nm). These superparamagnetic MNPs have significant impacts on T_2 of the samples according to their magnetization (M_s) attributed to their capability to perturb the local magnetic field homogeneity. When IgG is absent in the sample, the MNPs stay mono-dispersed inside the solution, yielding a T_2 of 258 ms. Consequently, when there is IgG in the samples, the Human IgG will cross-link with the Protein A on the MNPs, assembling nanoparticles micro-clusters. These micro-clusters, with a diameter d_c depending on the concentration of the target biomolecules, have a different magnetization M_C [43]:

$$M_C = M_S(\frac{d_c}{d_s})^{f-3} \quad (4)$$

with the fractal dimension of the micro-clusters f, and the diameter of a single MNP d_s. Accordingly, T_2 of the sample is commensurate with M_C. In this respect, T_2 is linked with the amount of IgG upon nanoparticles agglomeration. For instance, T_2 of the sample drops to 232.2 ms when the concentration of IgG is 12.5 nM inside the sample [Fig. 15(a)].

To evince the selectivity of the NMR-based biomolecule screening, chicken Immunoglobulin Y (IgY), which does not conjugate with the Protein A, is tested with the platform. T_2 from the samples has negligible change (<2%) from varying concentration of chicken IgY (5 to 50 nM), thus validating the selectivity of the assay.

Alternatively, by selecting the corresponding probe functionalized MNP, this versatile NMR-based screening scheme is capable of sensing widespread biomolecules. This is manifested by detection of DNA for life-threatening bacteria screening. With a similar sensing mechanism to the case for detecting human

IgG, the platform quantifies the synthesized DNA derived from *Enterococcus faecalis* by pair of probe-decorated MNPs (Ø: 100 nm). The Limit-of-Detection (LoD) for this platform, which is defined as $\Delta T_2 = 3\sigma$ above the blank sample, is estimated to be <100 pM [Fig. 15(b)]. Additionally, the dynamic range of the detection can be impelled to 125 nM of DNA by varying the concentration of the MNP (from 6.25 to 10 µg/mL). The response of the assay to single-nucleotide polymorphism is indistinguishable to T_2 baseline (<4%), substantiating the possibility of differentiation of a single-base mismatch DNA. The reason of DNA assay has a higher sensitivity compared to the IgG assay may attribute to the different size, number of binding site and relaxivity of the MNP. By optimizing these parameters, the detection limit of the micro-NMR platform can be further decreased to a fM level [43].

One of the unique features of the NMR is its capability to probe the molecular structure of the samples, which renders this micro-NMR platform a versatile tool for different areas of application. For instance, protein β-lactoglobulin (β-LG), which is a major protein found in milk products, has significant impacts on the texture as well as nutritional quality of the food [44]. β-LG exists as a native dimer at room temperature. When they experience heat >60 °C, β-LG denatures and aggregates as globules irreversibly. This state transformation decreases T_2 of the sample as the transverse relaxation of protons is sensitive to the aggregation. In fact, T_2 from the samples drops from 40% to 74% when heated to 95 °C according to their concentration [Fig. 15(c)]. Thus this T_2 deviation can indicate the state of the whey proteins of foods.

Similarly, the adoption of this platform allows the detection of the dynamics between the solvent and polymer for colloidal application. Poly(N-isopropylacrylamide) (PNIPAM), widely used as the advanced sensor and drug delivery carrier, demonstrates temperature-induced volume phase transition at lower critical solution temperature (~33 °C) in the water [45]. This phase transition affects the local environment in terms of solvent confinement and subsequently T_2 of the solvent. To diversify the capabilities of this platform, the NMR sensing coil is utilized as a thermal heater to perform thermal profiling on the PNIPAM. When the applied power to the heater is small (duty cycle ≤ 2%), the temperature

of the sample does not rise, and the PNIPAM stays in a swollen state. If the power is increased gradually (duty cycle ≥ 4%), the PNIPAM starts to undergo a volume phase transition. This collapsed state of PNIPAM confounds the mobility of bound water molecule then resulting in T_2 decrement of the solvent (~9%) [Fig. 15(d)]. The ability of sample thermal control is predominantly limited by the sample evaporation. In fact, adding a PDMS mold can prevent the sample evaporation and further increase the ability to heat the sample.

C. Comparison and Discussion

Table I compares this work with recent CMOS PoU tools. It supports multi-type assays in one unified platform, while achieving high sensitivity and selectivity for DNA, as well as other proteins targeting capability inside 2.5 µL sample with corresponding probe-decorated MNPs. The NMR-based sensing scheme eases the hardware and sample preparation for the assays (i.e., post-processing and probe-immobilization on CMOS, tag labelling on target, washing of magnetic particles) when compared to others such as fluorescent-/capacitive-sensing. While compared to the previous reported CMOS NMR systems, the B_0-field stabilization module here facilitates the electronics, and enhances the robustness of the platform (Table. II). Moreover, this micro-NNR platform includes a thermal module, which is an added feature to explore the thermal profile of the samples and opens up a broad range of possibilities for on-chip thermal analysis [46], [47]. Yet, due to the large sensing coil, the implementation of microarray for multiplex sensing is unfeasible. In addition, limited by the homogeneity of the magnet, NMR spectroscopy, as demonstrated by Ha *et al* [22], is not supported by this platform. Still, the NMR relaxometry applications demonstrated here render this platform as a promising candidate for PoU tool. A comparison with a commercial benchtop relaxometer shows that this platform consumes 120x fewer samples, and is 96x lighter, 175x smaller and 16x cheaper when evaluated against the selling price of [48], with a trade-off of

lower tuning range on sample temperature. Together with the proposed B_0-field stabilization scheme, that facilitates the operations, this system is in the vanguard of CMOS PoU tools.

V. Conclusions

By incorporating the Hall sensor and micro-NMR TRX, this paper described a handheld CMOS micro-NMR platform with effective closed-loop B_0-field stabilization, and evinced superiority of the NMR-based sensing for PoU assay from different points-of-view. In terms of applications this platform exhibited the utilization of a single CMOS chip to attain versatile sensitive chemical/biological assay from diverse unprocessed samples such as protein, DNA, and polymer. The LoD of the platform for *Enterococcus faecalis* derived DNA is <100 pM from a 2.5-µL sample using functionalized MNPs. The developed thermal module also extends the potential applications (e.g., polymer dynamics study). In terms of hardware, the micro-NMR platform reveals high robustness confirmed by the exploration of the current-mode Hall sensor and readout circuit in conjunction with a current driver to stabilize the B_0-field variation attributed to the environments. We anticipate that this handheld micro-NMR platform will help to popularize the application of NMR and magnify the advantages of NMR to our daily lives.

ACKNOWLEDGEMENT - Research funded by the Macao Science and Technology Development Fund (FDCT) under the project (047/2014/A1) and State Key Lab fund.

Reference:

[1] G. Gauglitz, "Point-of-care platforms," *Annu. Rev. Anal. Chem.,* vol. 7, pp. 297-315, Jun. 2014.

[2] P. Neužil, C. D. M. Campos, C. C. Wong, J. B. W. Soon, J. Reboud, and A. Manz, "From chip-in-a-lab to lab-on-a-chip: towards a single handheld electronic system for multiple application-specific lab-on-a-chip (ASLOC)," *Lab Chip*, vol. 14, no. 13, pp. 2168-2176, Jul. 2014.

[3] H. Shafiee, S. Wang, F. Inci, M. Toy, T. J. Henrich, D. R. Kuritzkes, and U. Demirci, "Emerging technologies for point-of-care management of HIV infection," *Annu. Rev. Med.*, vol. 66, pp. 387-405, Jan. 2015.

[4] World Health Organization. *Major causes of death* [online]. Available: http://www.who.int/mediacentre/factsheets/fs310/en/index2.html

[5] J. P. Lafleur, A. Jönsson, S. Senkbeil, and J. P. Kutter, "Recent advances in lab-on-a-chip for biosensing applications," *Biosens. Bioelectron.,* vol. 76, pp. 213-233, Feb. 2016.

[6] M. Zuiderwijk, H. J. Tanke, R. S. Niedbala, and P. L. A. M. Corstjens, "An amplification-free hybridization-based DNA assay to detect *Streptococcus pneumoniae* utilizing the up-converting phosphor technology," *Clin. Biochem.,* vol. 36, no. 5, pp. 401-403, Jul. 2003.

[7] G. A. Posthuma-Trumpie, J. Korf, and A. van Amerongen, "Lateral flow (immuno)assay: its strengths, weaknesses, opportunities and threats. A literature survey," *Anal. Bioanal. Chem.,* vol. 393, no. 2, pp. 569-582, Jan. 2009.

[8] S. K. Arya, C. C. Wong, Y. J. Jeon, T. Bansal, and M. K. Park, "Advances in complementary-metal–oxide–semiconductor-based integrated biosensor arrays," *Chem. Rev.*, vol. 115, no. 11, pp. 5116-5158, Jun. 2015.

[9] H. J. Yoo and C. van Hoof, *Bio-Medical CMOS ICs*. New York: Springer, 2011.

[10] B. Jang, P. Cao, A. Chevalier, A. Ellington, and A. Hassibi, "A CMOS fluorescent-based biosensor microarray," in *IEEE Int. Solid-State Circuits Conf. Dig. Tech. Papers (ISSCC)*, 2009, pp. 436–437.

[11] K.-H. Lee, S. Choi, J. O. Lee, J.-B. Yoon, and G.-H. Cho, "CMOS capacitive biosensor with enhanced sensitivity for label-free DNA detection," in *IEEE Int. Solid-State Circuits Conf. Dig. Tech. Papers (ISSCC)*, 2012, pp. 120–121.

[12] H. M. Jafari, K. Abdelhalim, L. Soleymani, E. H. Sargent, S. O. Kelley, and R. Genov, "Nanostructured CMOS wireless ultra-wideband label-free PCR-free DNA analysis SoC," *IEEE J. Solid-State Circuits*, vol. 49, no. 5, pp. 1223-1241, May 2014.

[13] D. A. Hall, J. S. Daniels, B. Geuskens, N. Tayebi, G. M. Credo, D. J. Liu, *et al.*, "A nanogap transducer array on 32 nm CMOS for electrochemical DNA sequencing," in *IEEE Int. Solid-State Circuits Conf. Dig. Tech. Papers (ISSCC)*, 2016, pp. 288–289.

[14] P.-H. Kuo, J.-C. Kuo, H.-T. Hsueh, J.-Y. Hsieh, Y.-C. Huang, T. Wang, *et al.*, "A smart CMOS assay SoC for rapid blood screening test of risk prediction," in *IEEE Int. Solid-State Circuits Conf. Dig. Tech. Papers (ISSCC)*, 2015, pp. 390-391.

[15] D. A. Hall, R. S. Gaster, K. A. A. Makinwa, S. X. Wang, and B. Murmann, "A 256 pixel magnetoresistive biosensor microarray in 0.18µm CMOS," *IEEE J. Solid-State Circuits*, vol. 48, no. 5, pp. 1290-1301, May 2013.

[16] R. Thewes, "Introduction to CMOS-based DNA microarrays," in *Smart sensor systems: emerging technologies and applications,* G. Meijer, K. Makinwa, and M. Pertijs, United Kingdom: John Wiley & Sons Ltd, ch. 6, 2014.

[17] L. Josephson, J. M. Perez, and R. Weissleder, "Magnetic nanosensors for the detection of oligonucleotide sequences," *Angew. Chem. Int. Ed.,* vol. 40, no. 17, pp. 3204-3206, Sep. 2001.

[18] J. M. Perez, L. Josephson, T. O'Loughlin, D. Högemann, and R. Weissleder, "Magnetic relaxation switches capable of sensing molecular interactions," *Nat. Biotechnol.*, vol. 20, no. 8, pp. 816–820, Aug. 2002.

[19] H. Lee, E. Sun, D. Ham, and R. Weissleder, "Chip-NMR biosensor for detection and molecular analysis of cells," *Nat. Med.*, vol. 14, no. 8, pp. 869-874, Aug. 2008.

[20] N. Sun, Y. Liu, H. Lee, R. Weissleder, and D. Ham, "CMOS RF biosensor utilizing nuclear magnetic resonance," *IEEE J. Solid-State Circuits,* vol. 44, no. 5, pp. 1629-1643, May 2009.

[21] N. Sun, T.-J. Yoon, H. Lee, W. Andress, R. Weissleder, and D. Ham, "Palm NMR and 1-chip NMR," *IEEE J. Solid-State Circuits,* vol. 46, no. 1, pp. 342-352, Jan. 2011.

[22] D. Ha, J. Paulsen, N. Sun, Y.-Q. Song, and D. Ham, "Scalable NMR spectroscopy with semiconductor chips," *Proc. Nat. Acad. Sci. (PNAS),* vol. 111, no. 33, pp. 11955-11960, Aug. 2014.

[23] K.-M. Lei, P.-I. Mak, M.-K. Law, and R. P. Martins, "A µNMR CMOS transceiver using a Butterfly-coil input for integration with a digital microfluidic device inside a portable magnet," *IEEE J. Solid-State Circuits,* to be published.

[24] K.-M. Lei, H. Heidari, P.-I. Mak, M.-K. Law, F. Maloberti, and R. P. Martins, "A handheld 50pM-sensitivity micro-NMR CMOS platform with B-field stabilization for multi-type biological/chemical assays," in *IEEE Int. Solid-State Circuits Conf. Dig. Tech. Papers (ISSCC)*, 2016, pp. 474–475.

[25] N. E. Jacobsen, *NMR spectroscopy explained*. New Jersey: John Wiley & Sons, Inc, 2007.

[26] G. A. Morris, H. Barjat, and T. J. Horne, "Reference deconvolution methods," *Prog. Nucl. Magn. Reson. Spectrosc.*, vol. 31, no. 2-3, pp. 197-257, Sept. 1997.

[27] Ē. Kupče, and R. Freeman, "Molecular structure from a single NMR sequence (fast-PANACEA)," *J. Magn. Reson.,* vol. 206, no. 1, pp. 147-153, Sept. 2010.

[28] K.-M. Lei, P.-I. Mak, M.-K. Law, and R. P. Martins, "A palm-size µNMR relaxometer using a digital microfluidic device and a semiconductor transceiver for chemical/biological diagnosis," *Analyst*, vol. 140, no.15, pp. 5129-5137, Aug. 2015.

[29] H. Y. Carr and E. M. Purcell, "Effects of diffusion on free precession in nuclear magnetic resonance experiments," *Phys. Rev.*, vol. 94, no. 3, pp. 630-638, May 1954.

[30] S. Meiboom and D. Gill, "Modified spin-echo method for measuring nuclear relaxation times," *Rev. Sci. Instrum.,* vol. 29, no. 8, pp. 688-691, Aug. 1958.

[31] S. D'Amico, M. Conta, and A. Baschirotto, "A 4.1-mW 10-MHz fourth-order source-follower-based continuous-time filter with 79-dB DR," *IEEE J. Solid-State Circuits,* vol. 41, no. 12, pp. 2713-2719, Dec. 2006.

[32] J. Watzlaw, S. Glöggler, B. Blümich, W. Mokwa, and U. Schnakenberg, "Stacked planar micro coils for single-sided NMR applications," *J. Magn. Reson.,* vol. 230, pp. 176-185, May 2013.

[33] J. Jiang, W. J. Kindt, and K. A. A. Makinwa, "A continuous-time ripple reduction technique for spinning-current Hall sensors," *IEEE J. Solid-State Circuits*, vol. 49, no. 7, pp. 1525-1534, Jul. 2014.

[34] H. Heidari, E. Bonizzoni, U. Gatti, and F. Maloberti, "A CMOS current-mode magnetic Hall sensor with integrated front-end," *IEEE Trans. Circuits Syst. I Regul. Pap.*, vol. 62, no. 5, pp. 1270-1278, May 2015.

[35] J. Jiang and K. Makinwa, "A hybrid multipath CMOS magnetic sensor with 210µT_{rms} resolution and 3MHz bandwidth for contactless current sensing," in *IEEE Int. Solid-State Circuits Conf. Dig. Tech. Papers (ISSCC)*, 2016, pp. 204–205.

[36] G.-M. Sung and C.-P. Yu, "2-D differential folded vertical Hall device fabricated on a P-type substrate using CMOS technology," *IEEE Sensors J.*, vol. 13, no. 6, pp. 2253-2262, Jun. 2013.

[37] C. Sander, M.-C. Vecchi, M. Cornils, and O. Paul, "From three-contact vertical hall elements to symmetrized vertical hall sensors with low offset," *Sens. Actuators, A,* vol. 240, pp. 92-102, Apr. 2016.

[38] D. Kim, B. Goldstein, W. Tang, F. J. Sigworth, and E. Culurciello, "Noise analysis and performance comparison of low current measurement systems for biomedical applications," *IEEE Trans. Biomed. Circuits Syst.*, vol. 7, no. 1, pp. 52–62, Feb. 2013.

[39] M. Crescentini, M. Bennati, M. Carminati, and M. Tartagni, "Noise limits of CMOS current interfaces for biosensors: A review," *IEEE Trans. Biomed. Circuits Syst.*, vol. 8, no. 2, pp. 278–292, Apr. 2014.

[40] K.-M. Lei, H. Heidari, P.-I. Mak, M.-K. Law, and F. Maloberti, "Exploring the noise limits of fully-differential micro-watt transimpedance amplifiers for Sub-pA/√Hz sensitivity," in *11th Conf. Ph.D. Res. Microelectron. Electron. (PRIME),* 2015, pp. 290-293.

[41] K. N. Leung and P. K. T. Mok, "Analysis of multistage amplifier-frequency compensation," *IEEE Trans. Circuits Syst. I,* vol. 48, no. 9, pp. 1041-1056, Sep. 2001.

[42] Datasheet of NMR permanent magnet PM-1055, [online]. Available: http://metrolab.com/wp-content/uploads/2015/07/PM1055_broch.pdf

[43] C. Min, H. Shao, M. Liong, T.-J. Yoon, R. Weissleder, and H. Lee, "Mechanism of magnetic relaxation switching sensing," *ACS Nano*, vol. 6, no. 8, pp. 6821-6828, Aug. 2012.

[44] L. Indrawati, R. L. Stroshine, and G. Narsimhan, "Low-field NMR: A tool for studying protein aggregation," *J. Sci. Food Agric.,* vol. 87, pp. 2207-2216, Sep. 2007.

[45] B. Sierra-Martín, J. R. Retama, M. Laurenti, A. F. Barbero*,* and E. L. Cabarcos, "Structure and polymer dynamics within PNIPAM-based microgel particles," *Adv. Colloid Interface Sci.*, vol. 205, pp. 113-123, Mar. 2014.

[46] D. H. Gultekin and J. C. Gore, "Temperature dependence of nuclear magnetization and relaxation," *J. Magn. Reson.*, vol. 172, no. 1, pp. 133-141, Jan. 2005.

[47] L. Vermeir, M. Balcaen, P. Sabatino, K. Dewettinck, P. V. der Meeren, "Influence of molecular exchange on the enclosed water volume fraction of W/O/W double emulsions as determined by low-resolution NMR diffusometry and T_2-relaxometry," *Colloids Surf., A,* vol. 456, pp. 129-138, Aug. 2014.

[48] Bruker Minispec Contrast Agent Analyzer, [online]. Available: https://www.bruker.com/products/mr/td-nmr/minispec-mq-series/mq-contrast-agent-analyzer/overview.html

Figure and Table Captions:

Fig. 1. Conceptual diagram of the proposed micro-NMR platform for PoU applications. Different samples such as protein and DNA can be directly put atop the CMOS chip for assays. A portable magnet is entailed to magnetize the nuclei inside the samples.

Fig. 2. System block diagram. The transmitter and receiver transduce between magnetic and electrical signals with a thermal-controlled spiral coil. The B_0-field sensor and calibrator automatically stabilize the bulk magnetization on the µL-sample. No frequency synthesizer is required.

Fig. 3. Timing diagram of the CPMG pulses, including the excitation pulses delivered to the TX to excite the nuclei and the response from the nuclei, which is picked up by the coil. Herein, the single LO architecture for the TRX guarantees in-phase excitation and echoes responses to obtain harmonized peak-amplitudes.

Fig. 4. (a) Simulated 3D temperature distribution of the droplet at applied power of 8 mW in COMSOL Multiphysics®; (b) Simulated droplet average temperature at applied power from 0 to 20 mW.

Fig. 5. The cross-section of a single VHS element and its current path. (a) Without lateral magnetic field; (b) with lateral magnetic field B_0.

Fig. 6. Proposed current-mode 4-folded VHS arranged in Wheatstone bridge to sense the lateral B_0-field and its readout circuit (spinning circuitry is omitted for simplicity). The latter features a nominal B_0-field compensator to offset the strong nominal B_0-field (0.46 T) for better sensitivity (3.75 mT). The green arrows highlight the current paths of I_{Hall}. Inset shows the timing diagram for the switches and overall operations.

Fig. 7. Illustration for the two-phase spinning technique on the VHS. The bias direction (U_1 and U_3) together with the output terminals (U_2 and U_4) of the VHS are swapped periodically to eliminate the 1/f noise and offset of the elements.

Fig. 8. Simulated frequency response of the TIA with various T_{INT}.

Fig. 9. Simulated channel resistance (R_{DS}) and parasitic capacitance (C_G+C_D) of the N-channel MOSFET versus channel width.

Fig. 10. Simulated output waveforms of the integrator. Without the nominal B_0-field compensator, the integrator is saturated due to the large current induced by the nominal B_0-field before it accumulates an adequate voltage difference. Whereas with the compensator, the nominal B_0-field can be compensated thus the integration time can be prolonged to produce sufficient voltage differences at the output.

Fig. 11. (a) Chip photo of the fabricated chip in 0.18-µm CMOS; (b) Prototype of the micro-NMR platform with B_0-field stabilization and Lab-on-a-chip feasibility for multi-type biological/chemical assays, including: 1) Permanent magnet; 2) CMOS micro-NMR chip (inside magnet); 3) PCB; 4) FPGA and 5) Current driver. (c) Experimental setup. A program developed in C# is entailed for hardware control and visualizing the experimental results. The platform is powered by two batteries for portability.

Fig. 12. Timing diagram of the B_0-field calibration and its frequency-domain illustration.

Fig. 13. (a) Measured Hall sensor response; (b) B_0-field with and without calibration. Actual B_0-field is the sum of the B_0-field from the permanent magnet and the auxiliary coil driven by the current driver.

Fig. 14. (a) Measured power consumption and FoM of the crystal oscillator at different supply voltages; (b) Measured phase noise of the crystal oscillator (V_{DD} = 0.9 V, f = 78.5 MHz). Compared to the LO generated from signal generator (Agilent 3350A), the crystal oscillator shows a much better phase noise at low power.

Fig. 15. Experimental results from biological/chemical samples. The experiments are repeated and averaged to enhance the SNR. Each scan starts 10 seconds after the previous scan for nuclei stabilization. Errors bars represent 95% confidence level for curve fitting. (a) Target quantification from human IgG as target and chicken IgY as control. (b) Target quantification from *Enterococcus faecalis* derived DNA together with single-base mismatch DNA. (c) Protein (β-LG) state detection with different heating temperature. (d) Polymer (PNIPAM) dynamics with the solvent during heating from the on-chip heater.

Table I. Summary and benchmark with other CMOS-based Point-of-Use systems.

Table II. Benchmark with previous CMOS NMR systems.

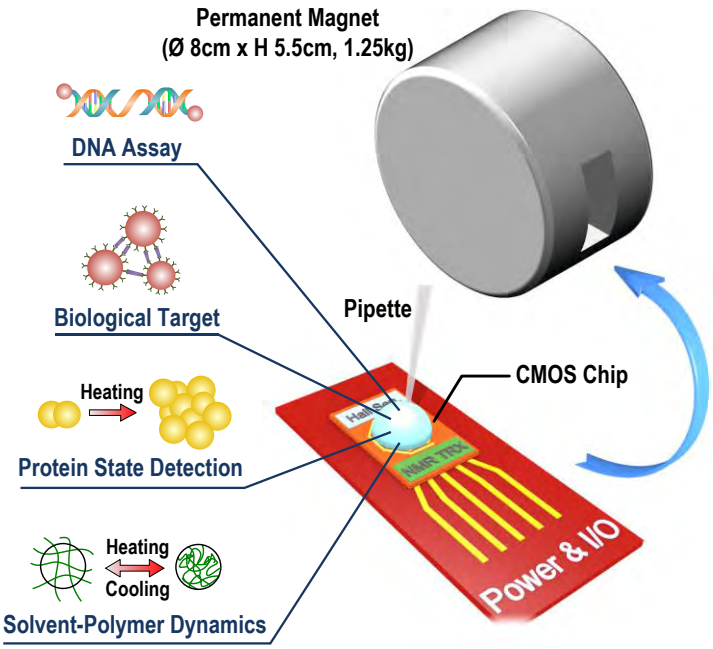

Fig. 1. Conceptual diagram of the proposed micro-NMR platform for PoU applications. Different samples such as protein and DNA can be directly put atop the CMOS chip for assays. A portable magnet is entailed to magnetize the nuclei inside the samples.

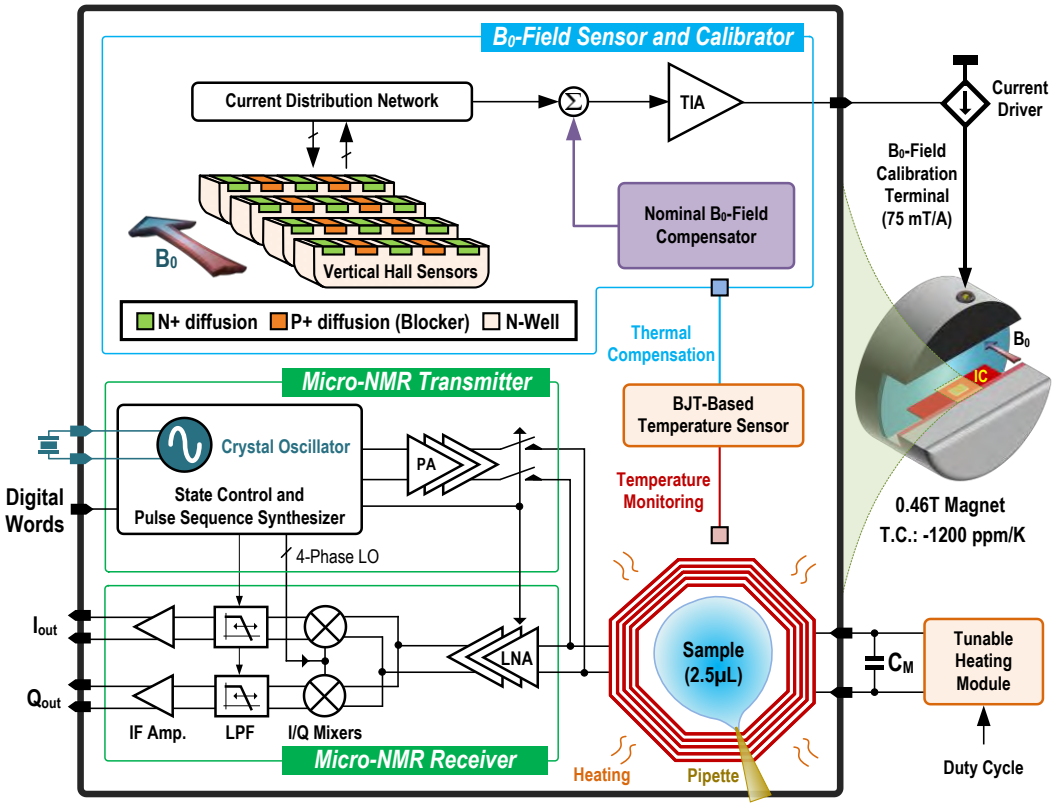

Fig. 2. System block diagram. The transmitter and receiver transduce between magnetic and electrical signals with a thermal-controlled spiral coil. The B_0-field sensor and calibrator automatically stabilize the bulk magnetization on the µL-sample. No frequency synthesizer is required.

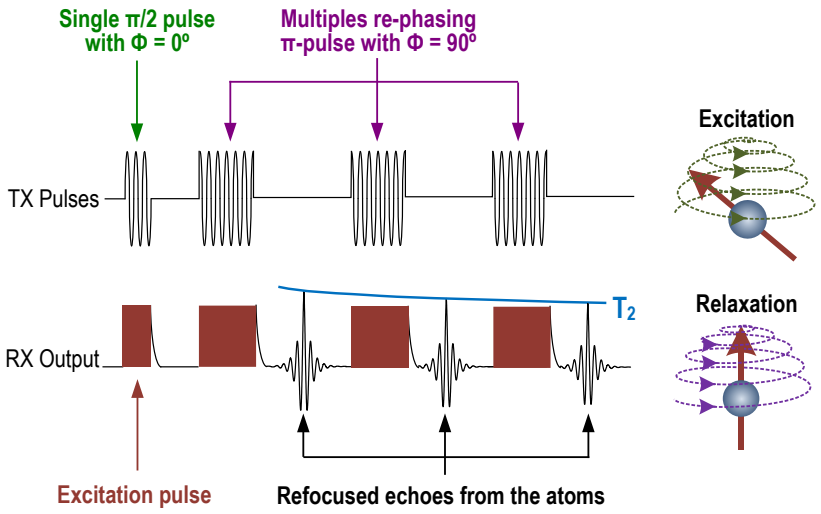

Fig. 3. Timing diagram of the CPMG pulses, including the excitation pulses delivered to the TX to excite the nuclei and the response from the nuclei, which is picked up by the coil. Herein, the single LO architecture for the TRX guarantees in-phase excitation and echoes responses to obtain harmonized peak-amplitudes.

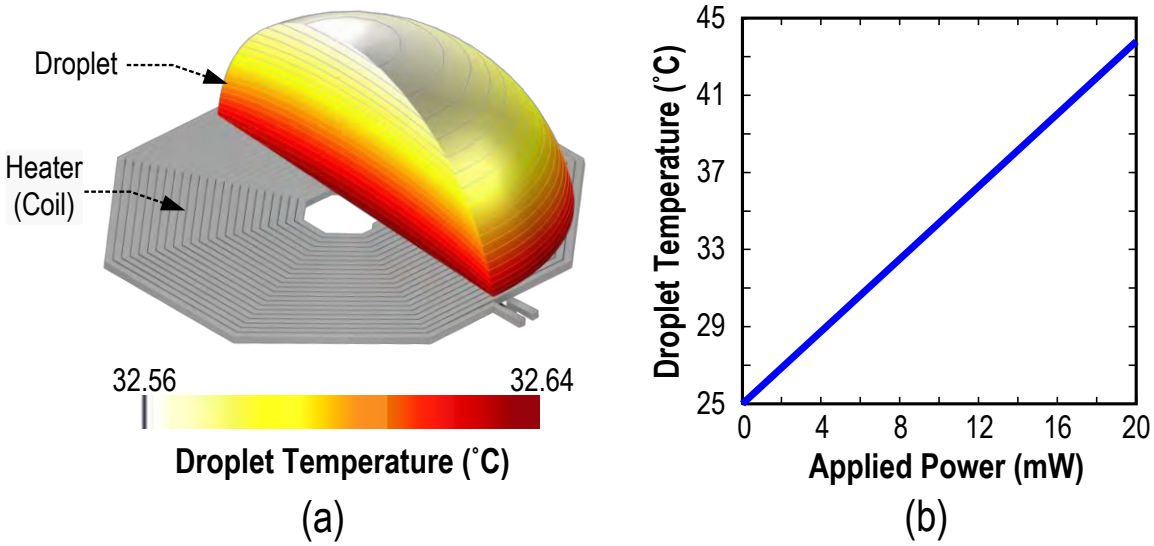

Fig. 4. (a) Simulated 3D temperature distribution of the droplet at applied power of 8 mW in COMSOL Multiphysics®; (b) Simulated droplet average temperature at applied power from 0 to 20 mW.

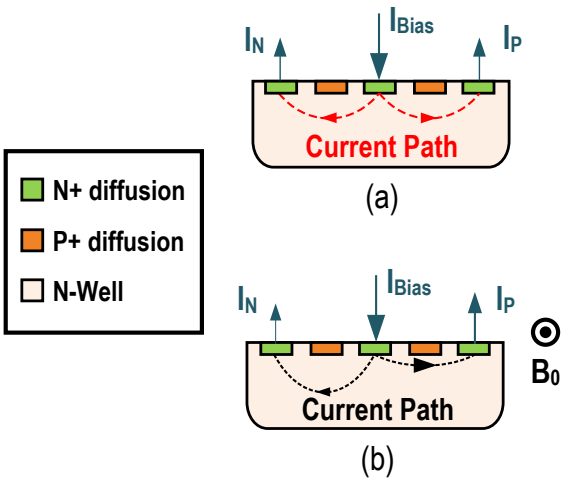

Fig. 5. The cross-section of a single VHS element and its current path. (a) Without lateral magnetic field; (b) with lateral magnetic field B_0.

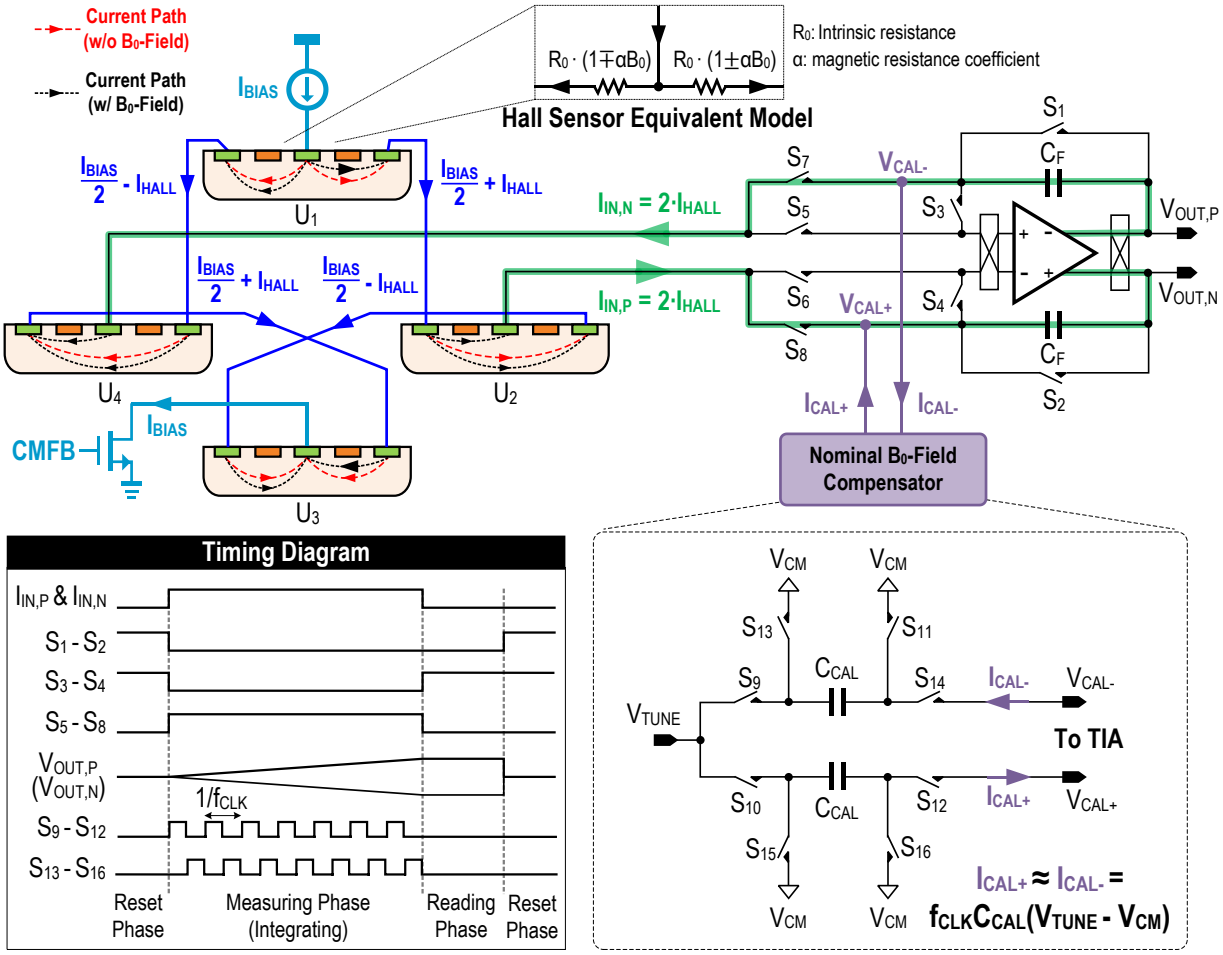

Fig. 6. Proposed current-mode 4-folded VHS arranged in Wheatstone bridge to sense the lateral B_0-field and its readout circuit (spinning circuitry is omitted for simplicity). The latter features a nominal B_0-field compensator to offset the strong nominal B_0-field (0.46 T) for better sensitivity (3.75 mT). The green arrows highlight the current paths of I_{Hall}. Inset shows the timing diagram for the switches and overall operations.

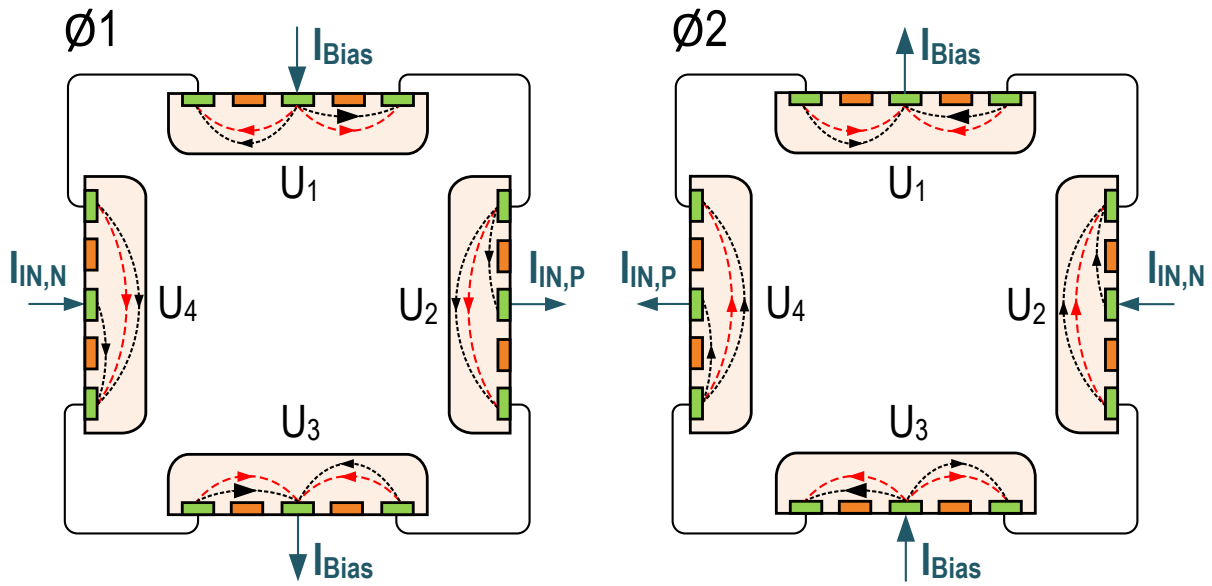

Fig. 7. Illustration for the two-phase spinning technique on the VHS. The bias direction (U_1 and U_3) together with the output terminals (U_2 and U_4) of the VHS are swapped periodically to eliminate the 1/f noise and offset of the elements.

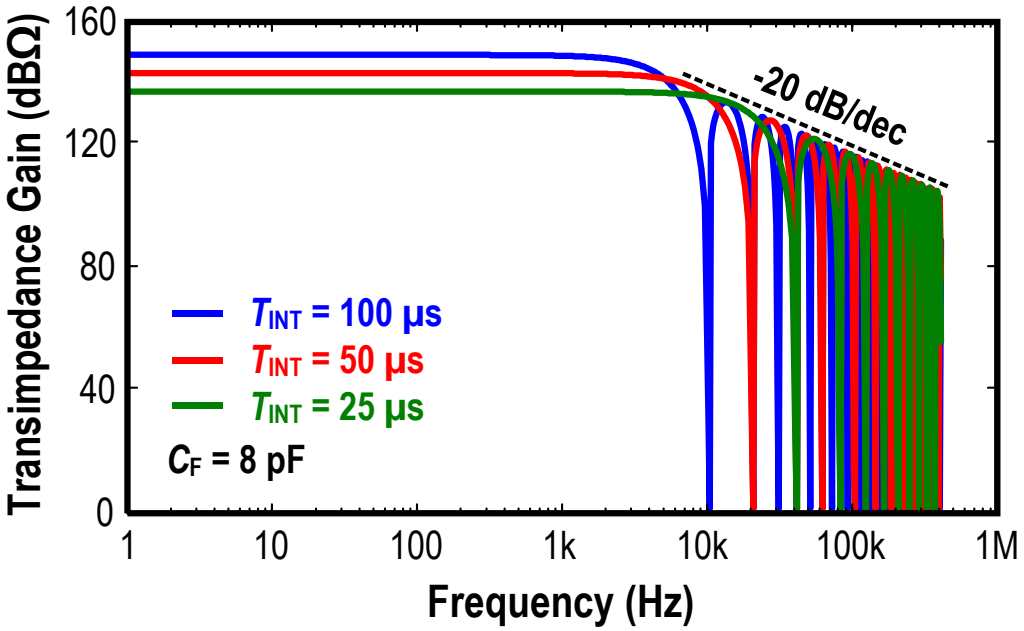

Fig. 8. Simulated frequency response of the TIA with various T_{INT}.

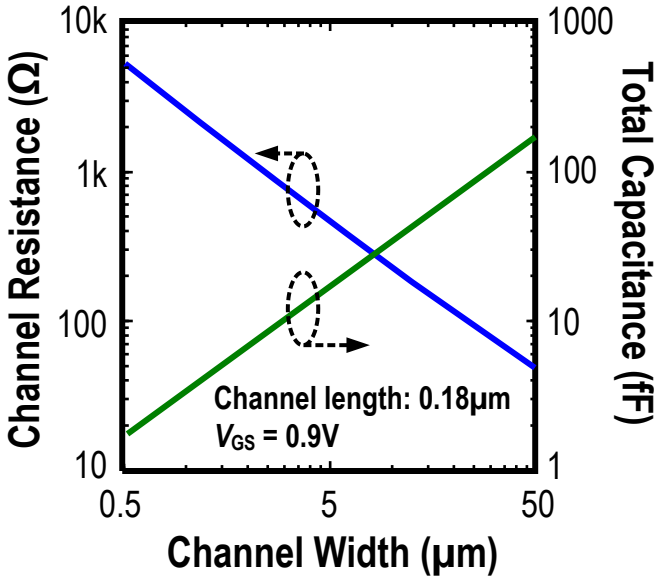

Fig. 9. Simulated channel resistance (R_{DS}) and parasitic capacitance (C_G+C_D) of the N-channel MOSFET versus channel width.

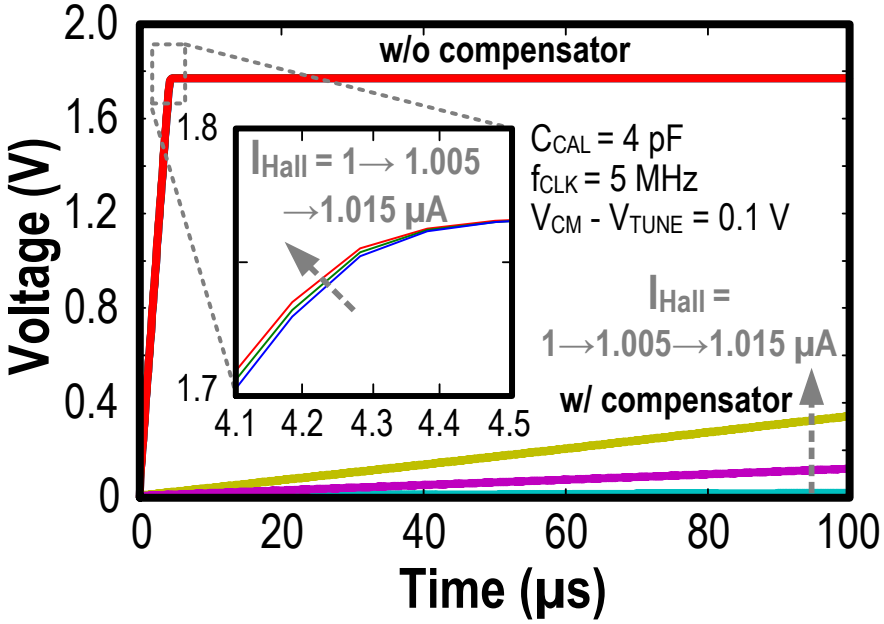

Fig. 10. Simulated output waveforms of the integrator. Without the nominal B_0-field compensator, the integrator is saturated due to the large current induced by the nominal B_0-field before it accumulates an adequate voltage difference. Whereas with the compensator, the nominal B_0-field can be compensated thus the integration time can be prolonged to produce sufficient voltage differences at the output.

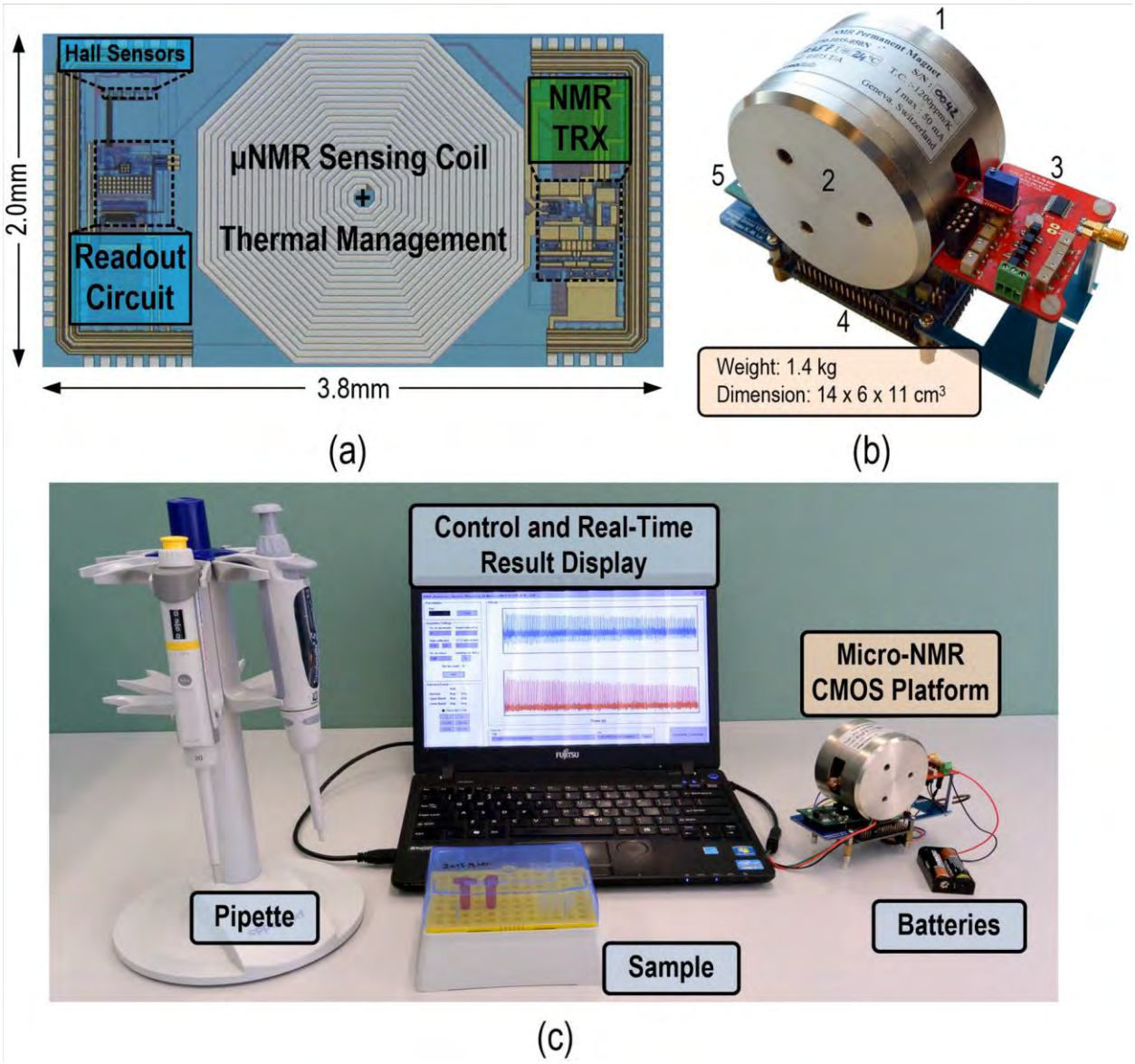

Fig. 11. (a) Chip photo of the fabricated chip in 0.18-μm CMOS; (b) Prototype of the micro-NMR platform with B_0-field stabilization and Lab-on-a-chip feasibility for multi-type biological/chemical assays, including: 1) Permanent magnet; 2) CMOS micro-NMR chip (inside magnet); 3) PCB; 4) FPGA and 5) Current driver. (c) Experimental setup. A program developed in C# is entailed for hardware control and visualizing the experimental results. The platform is powered by two batteries for portability.

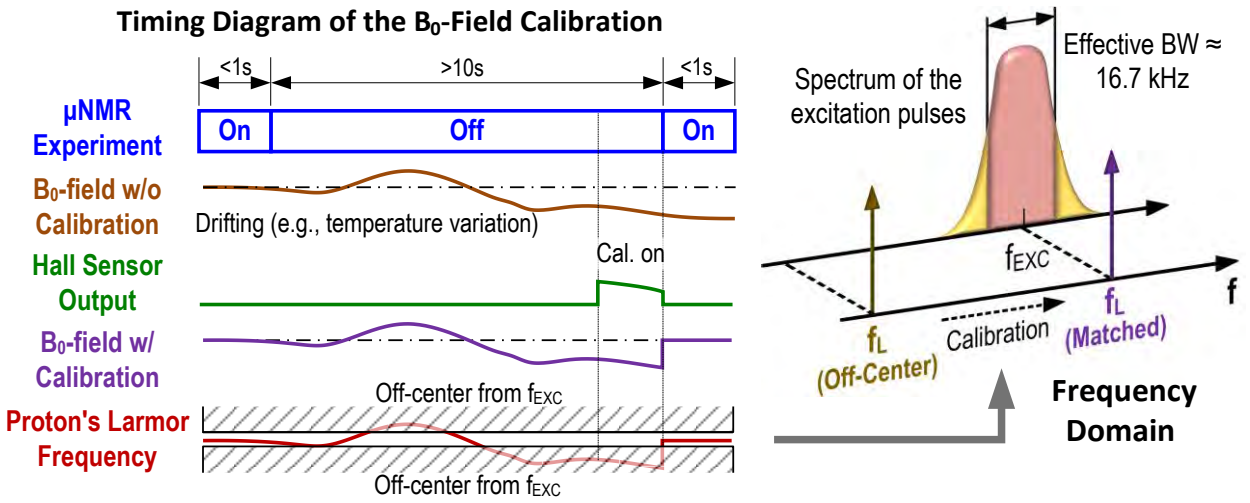

Fig. 12. Timing diagram of the B_0-field calibration and its frequency-domain illustration.

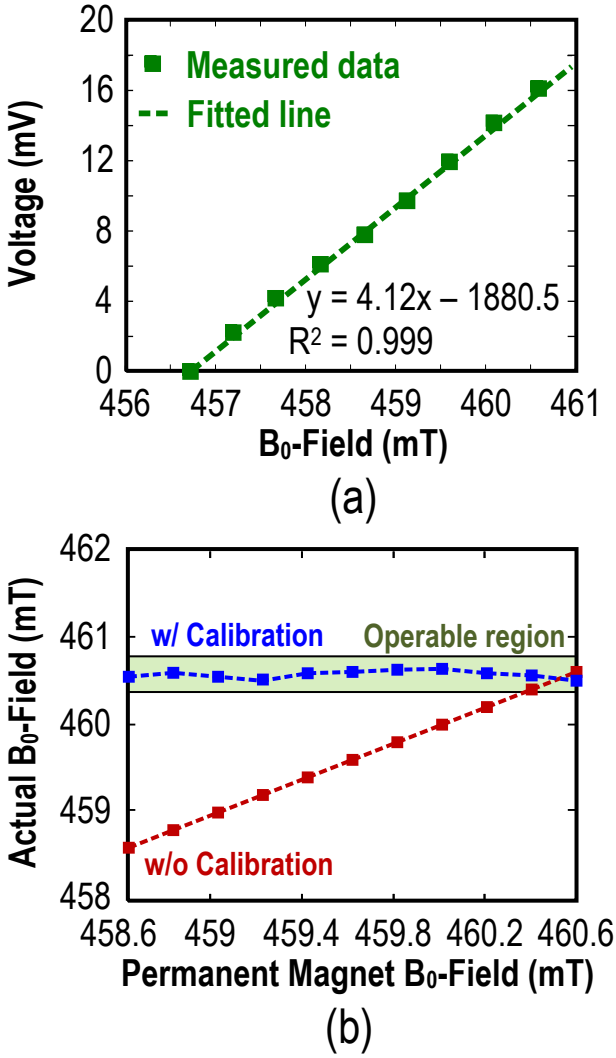

Fig. 13. (a) Measured Hall sensor response; (b) B_0-field with and without calibration. Actual B_0-field is the sum of the B_0-field from the permanent magnet and the auxiliary coil driven by the current driver.

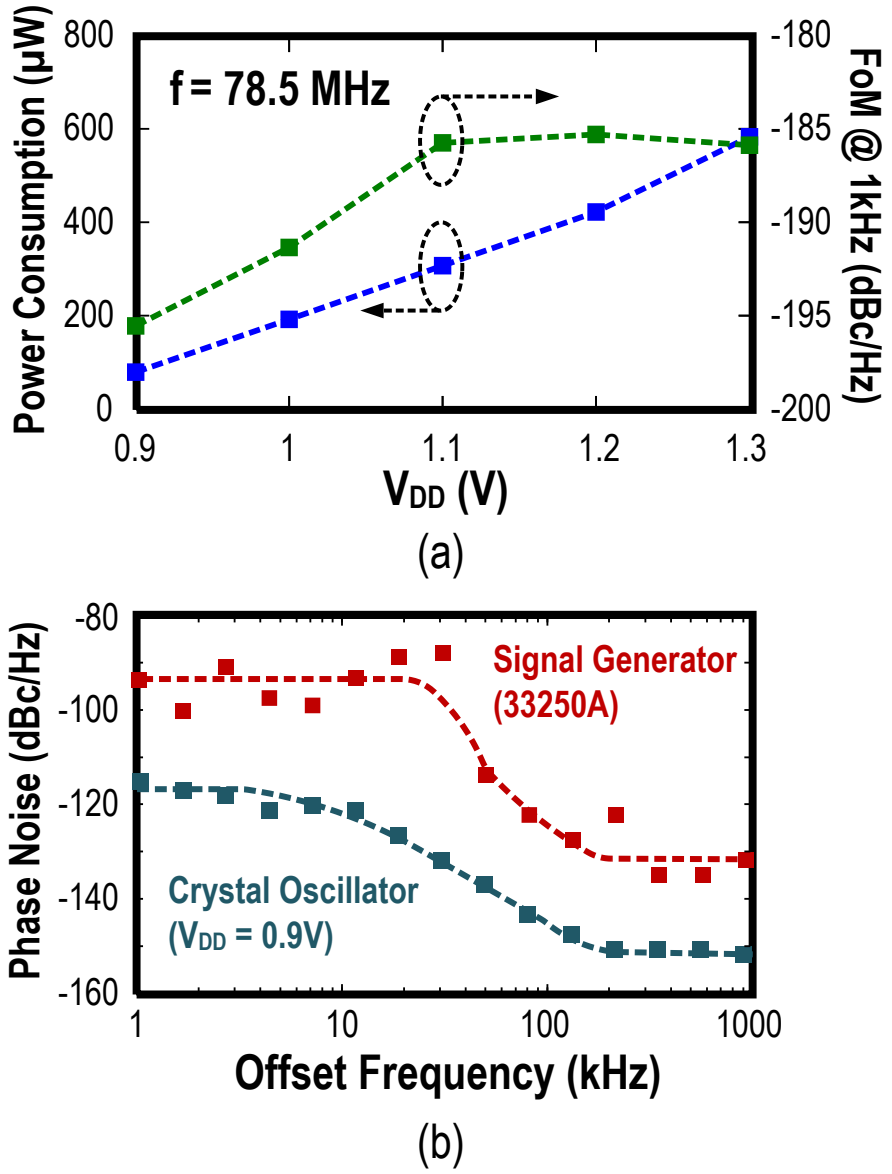

Fig. 14. (a) Measured power consumption and FoM of the crystal oscillator at different supply voltages; (b) Measured phase noise of the crystal oscillator (V_{DD} = 0.9 V, f = 78.5 MHz). Compared to the LO generated from signal generator (Agilent 3350A), the crystal oscillator shows a much better phase noise at low power.

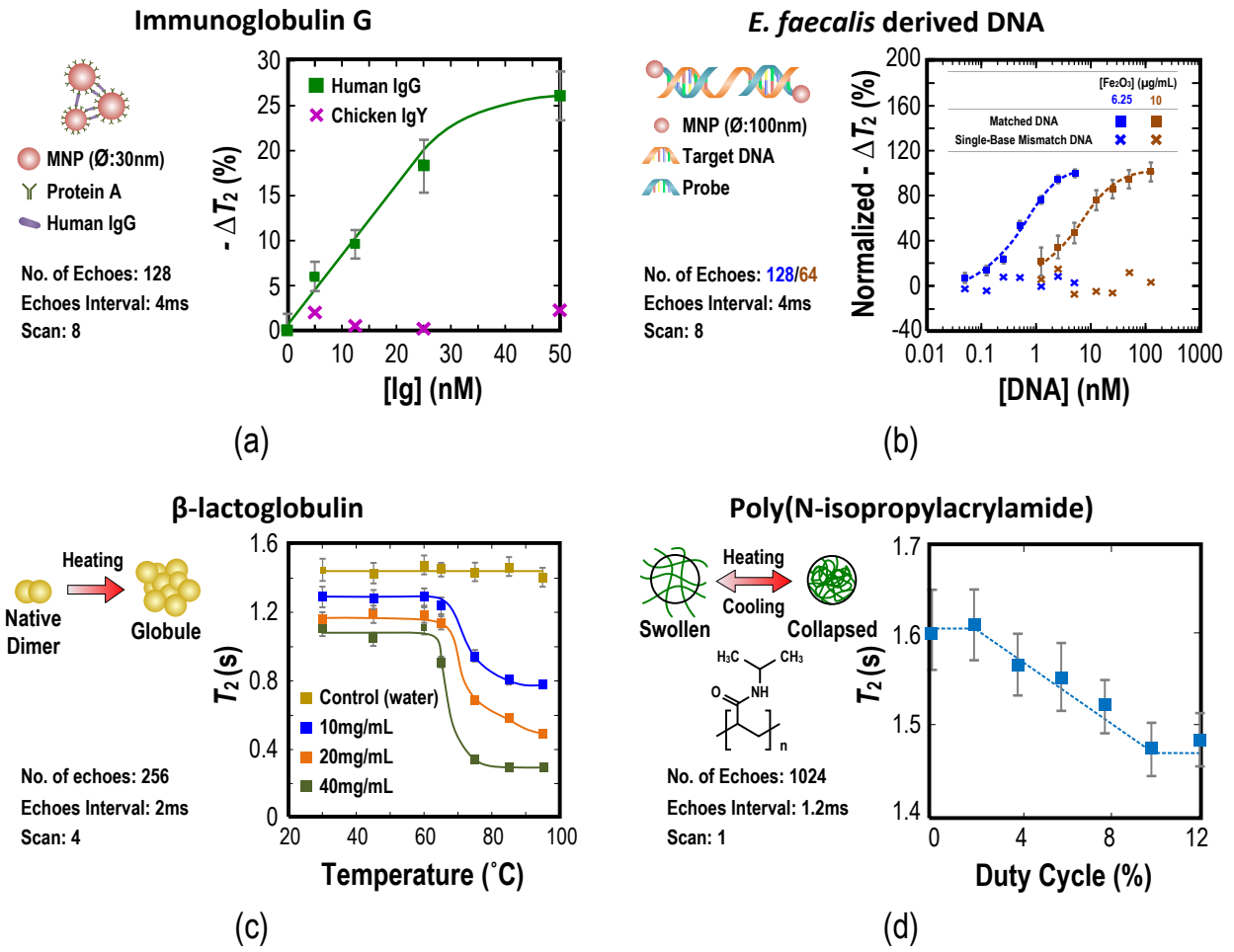

Fig. 15. Experimental results from biological/chemical samples. The experiments are repeated and averaged to enhance the SNR. Each scan starts 10 seconds after the previous scan for nuclei stabilization. Errors bars represent 95% confidence level for curve fitting. (a) Target quantification from human IgG as target and chicken IgY as control. (b) Target quantification from *Enterococcus faecalis* derived DNA together with single-base mismatch DNA. (c) Protein (β-LG) state detection with different heating temperature. (d) Polymer (PNIPAM) dynamics with the solvent during heating from the on-chip heater.

Table I. Summary and benchmark with other CMOS-based PoU systems.

	Sensing mechanism	No. of sensors	Demonstrated detection	Probe immobilization	Labeling	Technology (Chip area)
This work	**NMR relaxometry**	**1**	**DNA and protein detection**	**No**	**Quasi label-free**	**0.18 µm (7.6 mm²)**
[10]	Fluorescent-sensing	56	DNA detection	Yes	Cy3-label	0.35 µm (9.0 mm²)
[11]	Capacitive-sensing	54	DNA detection	Yes	Label-free	0.35 µm (20.0 mm²)
[12]	Cyclic voltammetry	12	DNA detection	Yes	Label-free	0.13 µm (9.0 mm²)
[14]	Magnetic-sensing	64	Protein detection	Yes	Quasi label-free	0.35 µm (8.9 mm²)
[15]*	Magnetic-sensing	256	Protein detection	Yes	Quasi label-free	0.18 µm (7.29 mm²)
[20]*	NMR relaxometry	1	Protein detection	No	Quasi label-free	0.18 µm (3.8 mm²)
[21]	NMR relaxometry	1	Protein and cell detection	No	Quasi label-free	0.18 µm (11.3 mm²)

**Off-chip sensors*

Table II. Benchmark with previous CMOS NMR systems.

		This Work	JSSC'09 [20]*	JSSC'11 [21]
Application	Specificity	**1. Target detection 2. Solvent-polymer dynamics 3. Protein state analysis**	Target detection	Target detection
	Demo target	**DNA/Human IgG**	Avidin	hCG cancer marker/ Bladder cancer cell
	Detection limit	**<100 pM# (DNA)**	5 nM (Avidin)	5 nM (Cancer marker)
	Sample handling limit	**2.5 µL**	5.0 µL	5.0 µL
Hardware	Physics	**NMR relaxometry + Thermal management**	NMR relaxometry	NMR relaxometry
	LO generation	**Crystal oscillator (Off-chip crystal)**	On-chip/Off-chip	Off-chip
	B_0-field calibration	**Yes**	No	No
	CMOS tech.	**0.18 µm**	0.18 µm	0.18 µm
	Chip area	**7.6 mm²**	3.8 mm²	11.3 mm²

**Off-chip sensors*

#50 pM reported in [24] with 95 % confidence level.